CetZ1-dependent polar assembly of the motility machinery in haloarchaea

Hannah J. Brown[1], Md Imtiazul Islam[2], Juanfang Ruan[2,3], Matthew A. B. Baker[2], Solenne Ithurbide[1,4], Iain G. Duggin[1#]

[1]Australian Institute for Microbiology and Infection (AIMI), University of Technology Sydney, Ultimo NSW 2007, Australia

[2]School of Biotechnology and Biomolecular Sciences (BABS), University of New South Wales, Kensington NSW 2052, Australia

[3]Electron Microscope Unit, Mark Wainwright Analytical Centre, UNSW Sydney, Kensington NSW 2052, Australia

[4]Present address: Département de Microbiologie, Infectiologie et Immunologie, Université de Montréal, Montréal, QC, Canada.

[#]Correspondence: Iain.Duggin@uts.edu.au

Abstract

Archaeal CetZ cytoskeletal proteins are a major group of the tubulin superfamily involved in the development of motile rod-shaped cells. In the model archaeon *Haloferax volcanii*, it has been unknown whether CetZs contribute to motility solely through the effects of rod cell shape on swimming speed, or in other ways too. Here, we used cryo-electron and fluorescence microscopy to observe cell surface filaments and the assembly of the motility machinery in cells carrying *cetZ1* or *cetZ2* deletion, overexpression, or dominant GTPase-deficient mutations. CetZ1 was found to play important roles in the polar assembly of motility marker proteins, including ArlD1, a constituent of the archaellum base, the chemotaxis sensory array adapter CheW1, and signal transducer CheY. Notably, overexpression of *cetZ1* reduced motility and the assembly of the motility machinery markers but did not affect the rod shape of motile cells. Dual protein localization studies further suggested that CetZ1 is not a direct stoichiometric component of the motility machineries but promotes their assembly via a significant role in organisation or structure of the cell poles.

Significance

This study demonstrates that cytoskeletal proteins (CetZs) can contribute to assembly of the motility machinery in archaea. In the model organism, *H. volcanii*, this function is expected to contribute significantly to the overall impact of CetZ1 on swimming motility, in addition to its established role in rod cell formation generating a streamlined shape. Our study also provides the first evidence that archaeal CetZ tubulin superfamily proteins can have structural or organisational roles for the assembly of protein complexes on the cell surface and cell poles. The multiple functions and subcellular locations of CetZ1 during motile cell development are reminiscent of eukaryotic cytoskeletal proteins and the roles of tubulin in basal bodies during the development of the eukaryotic flagellum.

Introduction

Cytoskeletal proteins are utilised as platforms or scaffolds for large protein complexes across the tree of life. Tubulin superfamily proteins are particularly widespread across all three domains, including tubulin in Eukarya, FtsZ in Bacteria and Archaea, and the Archaea-specific CetZ family [1-5]. In eukaryotes tubulin forms microtubules, which act as platforms in several different biological contexts, including for the anchoring and partitioning of chromosomes during cell division [6], intracellular transport of cargo [7,8] and assembly of protein complexes [9] and surface appendages [10]. In bacteria, FtsZ forms a ring at mid-cell which is an essential platform required for the assembly of the divisome complex, consisting of more than thirty proteins [11]. In comparison to tubulin and FtsZ, CetZs are understudied in terms of their basic biological functions and their capacity to act as platforms or scaffolds for assembly of other protein complexes.

In the motile and pleomorphic model halophilic archaeon, *Haloferax volcanii*, CetZs have been shown to control cell shape changes and have also been implicated in swimming motility [12,13]. *H. volcanii* has six CetZ paralogues, with CetZ1 and CetZ2 being the most highly conserved CetZs, and the only CetZs which have been functionally investigated. CetZ1 has a necessary role in rod-development, a morphological change which occurs in several conditions, including trace metal depletion [14], in early log phase growth, and when cells are motile [12,14]. Deletion of *cetZ1* and mutation of its GTPase active site (*cetZ1*.E218A), which is critical for CetZ1 polymerisation, both result in inhibition of rod-development [12,13]. Importantly, deletion and mutation of *cetZ1* also causes a severe motility defect [12].

Deletion of *cetZ2* has not yet been shown to result in a cell shape or motility phenotype [12], although expression of a *cetZ2* point mutant with an inactive GTPase domain prevents rod formation and causes a motility defect in a dominant inhibitory manner [12]. In addition to these observed motility phenotypes in *H. volcanii*, a survey of CetZs, motility, and rod shape across Haloarchaea found that the presence of both CetZ1 and CetZ2 in Haloarchaea species is highly correlated with motility and rod-shape [15]. With our current knowledge, the role of CetZs in motility is seemingly connected to their dominant function in cell shape control. It is not yet clear whether CetZs only contribute to motility through their control of rod-development, or whether they also participate in other mechanisms to promote swimming motility.

CetZ1 appears as dynamic structures around the cell envelope as motile rod cells take shape, and then forms a cap or patch-like structures at the cell poles later in rod development. In mature motile rods sampled from motility agar, the polar CetZ1 structures appeared especially bright and stable at the poles [12,13,16]. As CetZs are hypothesised to be multifunctional [15], one possibility is that they may contribute to the assembly or positioning of motility protein complexes, such as the archaellum or chemosensory arrays, at cell poles, after their role in rod shape development. Like in bacteria, archaeal chemotaxis arrays are responsible for sensing extracellular signals and activating a signal cascade that results in a change in rotational direction of the archaellum [17-19], the whip-like structure equivalent to the bacterial flagellum (reviewed in [20-24]). On a molecular level, chemotaxis proteins in Haloarchaea are like the bacterial system, with methyl-accepting chemotaxis proteins (MCPs), CheW, and CheA organised as a chemosensory array at the cell envelope. When extracellular signals bind to the

MCPs they induce a signal cascade that results in autophosphorylation of CheA, which in turn phosphorylates CheY [18]. Phosphorylated CheY shuttles between chemosensory arrays and the archaellum base (composed of ArlD and ArlCE) where it binds and phosphorylates CheF [17,19]. Together, ArlD and ArlCE are responsible for signal transduction to the archaellum motor proteins (ArlH, ArlI, ArlJ) and highly depend on these motor proteins for localization at the cell poles [18]. ArlD and ArlCE are thought to directly bind the archaellum motor [25,26] but are also presumed to bind a hypothesized polar cap or cytoplasmic cone structure at the cell poles [18]. MinD4, a homologue of bacterial MinD, also has a role in in the positioning of the archaellum and chemotaxis proteins at cell poles [27].

Polar caps are large cytoplasmic structures which are situated adjacent to the inner membrane in motile euryarchaea. They have been identified in *Pyrococcus furiosus* [26], *Thermococcus kodakarensis* [25], and *Halobacterium salinarum* [28]. The polar caps were found to act as polar organising centres associated with archaella bundles. In *P. furiosus* and *T. kodakarensis*, polar caps were also associated with chemosensory arrays. A polar cap has not yet been defined in *H. volcanii*, and the proteins which compose polar caps in euryarchaea are not yet known. Since CetZ proteins influence cell shape, particularly during rod cell development, and show complex localization patterns at midcell and along the cell length and eventually cell poles during motile rod development [12], here we investigated the potential for CetZ proteins to contribute to motility via assembly and positioning of polar archaellum and chemotaxis complexes.

Results

CetZ1 and CetZ2 differentially influence motility independently of cell shape control

CetZ1 and CetZ2 have previously been implicated in the control of cell motility [12], however it is not yet clear whether they solely contribute to motility through their control of cell shape, or whether they can influence motility independently of cell shape. To begin to investigate this, we measured the effects of *cetZ1* and *cetZ2* deletion and overexpression on motility in soft-agar, where cells swim out from a central inoculation site forming a halo (Fig. 1a). We also assessed the shape of motile cells withdrawn from the leading edge of the halo by image analysis of cell circularity, which is inversely related to cell elongation (Fig. 1b).

Deletion of *cetZ1* caused a severe motility defect, approximately 12% of wildtype motility (Fig. 1a), and prevented rod-formation in cells extracted from the leading edge of motility halos (Fig 1b), as previously reported with a different genetic background [12]. Importantly, overexpression of *cetZ1* in the wildtype or Δ*cetZ1* background reduced motility to approximately 75% of the wildtype control (carrying the vector only), despite cells at the leading edge still forming rods to the same degree as wildtype (Fig. 1a, b, Fig. S1a).

Deletion of *cetZ2* was previously reported to have no effect on motility or rod shape [12], which was confirmed here in motile cells (Fig. 1a). However, we also discovered that overexpression of c*etZ2*, whether in wildtype or Δ*cetZ2* backgrounds, resulted in a mild increase in motility, approximately 115% of wildtype (Fig. 1a). This also did not result in a clear change in cell shape (Fig. 1b).

We also investigated the interdependency of the overexpression phenotypes (Fig. S1a). Overexpression of *cetZ1* in the Δ*cetZ2* background caused reduced motility like it did in the wildtype background, indicating that the effects of *cetZ1* are independent of *cetZ2*. On the other hand, overexpression of *cetZ2* in the Δ*cetZ1* background failed to rescue the Δ*cetZ1* motility defect and did not clearly stimulate motility. Overexpression of the GTPase (T7 loop) mutants (*cetZ1*.E218A and *cetZ2*.E212A) inhibited motility and rod shape in the wildtype (H26) background, as previously reported in H98 [12], and had consistent effects in the *cetZ1* and *cetZ2* deletion strains (Fig. S1), suggesting that GTPase activity is necessary for the overexpression phenotypes of *cetZ1* and *cetZ2*.

The above experiments indicated that CetZs can promote motility independently of the rod shape of the mature motile cells. This led us to hypothesize that CetZs influence the assembly or function of other cell envelope or motility structures such as the archaellum or chemosensory arrays.

CetZ1 and CetZ2 influence the frequency of cell surface filaments

To investigate whether CetZs influence the overall appearance of surface filaments such as pili and archaella, we used cryo-EM (Fig. 1c) to compare the wildtype, *cetZ1* deletion and *cetZ2* overexpression strains, which showed the most substantial and opposing effects on motility, above. Deletion of *cetZ1* resulted in a significant reduction in the number of surface filaments per cell, whereas overexpression of *cetZ2* resulted in slightly more (Fig. 1d). As deletion of *cetZ1* and overexpression of *cetZ2* did not affect surface adhesion (Fig. S2), we hypothesized that these differences in the number of surface

filaments likely reflects differences in the number of archaella as opposed to pili, consistent with the observed motility phenotypes of these strains.

By comparing surface filament frequency in rods and plate-shaped cells, we found that in the rod-forming wildtype and *cetZ2* overexpression strains, rod-shaped cells had significantly more surface filaments compared to plate-shaped cells (Fig. 1e), suggesting as expected that cell shape correlates with the assembly of surface filaments. Interestingly, the number of surface filaments in the Δ*cetZ1* strain was still lower than the number of surface filaments in plate-shaped wildtype cells (Fig. 1d, e). Plates can be motile as shown by timelapse imaging of Δ*cetZ1* on soft-agar over an extended period of time, albeit with reduced speeds [12]. These observations suggest that the motility defect of Δ*cetZ1* is not only linked to its rod shape defect, but also a reduction in surface filaments such as the archaellum.

Functional CetZ-mTq2 fusions localise to cell poles in motile cells

CetZ1 was initially reported to localise strongly to cell poles in rod-shaped cells [12]. However, since the CetZ1-GFP fusion was not fully functional as a sole copy in rod-development, it remained unclear whether the polar localization reflected a native function of CetZ1. Subsequent studies of CetZ1 localization using an almost fully functional CetZ1-mTurquoise2 (mTq2) fusion have not investigated CetZ1 localization in motile cells [13,16]. Therefore, we next used the existing CetZ1-mTq2 fusion and generated a CetZ2-mTq2 fusion to observe the localizations of CetZ1 and CetZ2 in motile cells extracted from the leading edge of soft-agar motility halos.

CetZ1-mTq2 and CetZ2-mTq2 were first tested for their capacity to support motility in their respective *cetZ* knockout backgrounds (Fig. 2). CetZ1- and CetZ2-mTq2 fusions produced motility halos that were on average 71% and 107% of the size of those produced by expression of untagged *cetZ1* and *cetZ2*, respectively (Fig. 2a). These differences in motility were statistically significant between Δ*cetZ1*+*cetZ1* and Δ*cetZ1*+CetZ1-mTq2, but not between Δ*cetZ2*+*cetZ2* and Δ*cetZ2*+CetZ2-mTq2. Neither CetZ1-mTq2 nor CetZ2-mTq2 had a substantial effect on the shape of motile rods when expressed in the wildtype or knockout backgrounds (Fig. 2b).

In motile cells extracted from the halo edge, both proteins displayed bright patches at the cell poles (Fig. 2c-e). CetZ1-mTq2 showed additional patchy localization around the envelope and at mid-cell, like previously described (Fig. 2c) [12,13,16]. These similarities and differences in CetZ1-mTq2 and CetZ2-mTq2 localizations were clearly reflected in heat map representations of foci localization along normalized longitudinal and lateral cell axes (Fig. 2d). No differences in localization were observed when either CetZ-mTq2 fusion was expressed in the wildtype or their respective knockout genetic background.

CetZ1 strongly promotes the assembly of ArlD1-GFP

Given the above results, we sought to determine whether deletion of *cetZ1* or *cetZ2* or overexpression of the wildtype or GTPase mutants affect the assembly or positioning of key motility marker proteins. These included ArlD1 as a marker for the archaellum base, CheW1 as a marker for chemosensory arrays, and CheY, the effector protein that shuttles between chemosensory arrays and the archaellum base. Their localization in motile cells

198 have been previously well characterised [17,18] and expression of ArlD1-GFP, GFP-CheW1,
199 and CheY-GFP did not cause motility or cell shape changes (Fig. S3).

200 We sampled motile cells of the various strains expressing the markers from the leading
201 edge of soft agar halos for fluorescence microscopy. We assessed the degree of
202 assembly by counting the number of marker foci per cell. We assessed the subcellular
203 positioning of the foci by determining the percentage of foci located at the poles, and by
204 generating heatmaps representing the frequency of foci in a normalized cell shape of the
205 population. We also measured the local curvature around the outline of each cell and
206 determined its correlation with local fluorescence intensity (as shown in Fig. S4).

207 In wildtype motile cells, ArlD1-GFP localised as one or two foci of variable intensities at
208 the cell poles (Fig. 3a), like previously observed [17]. The cells showed a spread of mostly
209 elongated (rod) morphologies (Fig. 3a, 3d), most commonly with two foci per cell (Fig. 3e).
210 Cells with two or more foci tended to show a somewhat more elongated cell shape than
211 the single- or zero-focus cells (Fig. S6a). The average degree of cell elongation varied
212 somewhat between replicate halo samples (Fig. S6d), which is due to the sensitivity of
213 the known sharp transition to plate shaped cells seen when cells are sampled just inside
214 the outermost halo edge in soft agar [12]. Nevertheless, the great majority of detected
215 ArlD1-GFP foci were still located at the cell poles (>97%, Fig. S5b), as indicated in the
216 heatmap in Fig. 3g (left). Consistent with this, the local cell curvature strongly correlated
217 with fluorescence (Fig. 3f, upper graph).

218 The Δ*cetZ1* background showed the expected poor motility and failed to form rods (Fig.
219 3b-d) [12]. The rounder shape of these cells was also reflected by a reduced spread
220 (standard deviation) of curvature of the whole cell outlines compared to the wildtype (Fig.
221 S5a). Interestingly, in the Δ*cetZ1* background, most cells showed no ArlD1-GFP
222 localization or only one focus adjacent to the edge of the cell (Fig. 3b, 3e, S3g). There was
223 no clear correlation on average between local cell curvature and ArlD1-GFP localization
224 around the cell outline (Fig. 3f), although the foci position heatmap indicated a moderate
225 tendency of the detected foci to be located at the ends of the slightly longer of the two
226 cell axes (Fig. 3a, 3g).

227 When *cetZ1* was overexpressed, motile cells showed the normal rod morphology (Fig. 3b,
228 3d) and yet the number of ArlD1-GFP foci (Fig. 3e) and the average correlation of
229 fluorescence with cell curvature (Fig. 3f) was reduced compared to the wildtype
230 background. This is consistent with the moderately reduced swimming motility of this
231 strain (see Fig. 1a, 3c, 3d). The negative response of a phenotype to overexpression may
232 seem at first glance counterintuitive but is not uncommon [29].

233 Expression of the GTPase-deficient *cetZ1*.E218A mutant, which hyper-stabilizes the
234 protein filaments [12], inhibits rod formation and results in a heterogeneous population of
235 irregularly shaped cells. At relatively high overexpression levels it also causes cell
236 enlargement, signifying an interference with division (e.g., Fig. 3b, S1). In the infrequent
237 substantially enlarged cells, ArlD1-GFP localised as many foci distributed throughout the
238 cell and not at the cell edges (Fig. S3g), whereas the smaller cells showed low or no
239 localized fluorescence. This was seen as a decrease in the average number of ArlD1-GFP
240 foci per cell and a more skewed distribution (Fig. 3e) compared to the wildtype. There was
241 also a moderate negative correlation on average between the localization of ArlD1-GFP

242 and membrane curvature (Fig. 3f). Overexpression of *cetZ1*.E218A thus strongly
243 interferes with the assembly and positioning of ArlD1-GFP foci.

244 ***cetZ2 overexpression influences the assembly of ArlD1-GFP***

245 Deletion of *cetZ2* (Fig. 3b) had no detected effect on the assembly (Fig. 3e) or positioning
246 of ArlD1-GFP foci at the cell poles (Fig. 3f, 3g, S5b), consistent with the normal motility
247 and cell shape phenotypes exhibited by Δ*cetZ2* (e.g., Fig. 1a, 1b) [12]. When *cetZ2* was
248 overexpressed (Fig. 3b), ArlD1-GFP assembly at cell poles was moderately reduced (Fig.
249 3b, 3f, 3g, S5b), and showed less foci per cell (Fig. 3e), despite its slightly elevated motility
250 and number of surface filaments (Fig. 1). A possible explanation is that the increased
251 number of surface filaments (presumably archaella) were not reflected in the ArlD1-GFP
252 imaging due to close clustering of archaella at the poles.

253 Expression of the *cetZ2*.E212A GTPase mutant resulted in a milder cell shape effect than
254 *cetZ1*.E218A [12], where rod shape was inhibited but the plate-like cells were not highly
255 irregular or enlarged (e.g. Fig. 3b, S1b, S1c). Under these conditions, ArlD1-GFP appeared
256 as infrequent foci that were often not associated with the cell edge (Fig. 3b, 3e) and
257 showed a slight negative correlation with cell curvature on average (Fig. 3f). Thus, like
258 *cetZ1*.E218A, overexpression of *cetZ2*.E212A strongly interferes with the positioning of
259 ArlD1-GFP.

260 Since *cetZ2* deletion showed no impact on ArlD1-GFP positioning or assembly, these
261 results suggest that *cetZ2* is not substantially involved in archaellum assembly or motile
262 rod development under the standard conditions investigated. Overexpression of *cetZ2*
263 appears to mildly stimulate aspects of motility and reduced others via unknown
264 mechanisms.

265 ***CheW1 assembly is highly dependent on CetZ1***

266 In the wildtype background, GFP-CheW1 localized as expected [17] to polar and subpolar
267 regions as multiple foci or patches/filaments (Fig. 4a). Most of the cells were rods, with a
268 small fraction of plate-shaped cells in these samples (Fig. 4a, 4d), and we observed that
269 cells with more foci tended to show greater elongation (Fig. S6b).

270 Strikingly, deletion of *cetZ1* resulted in a diffuse signal for GFP-CheW1, with only a very
271 small proportion of cells displaying distinct faint foci (Fig. 4b, 4e) compared to the
272 typically 1-3 or more bright polar/subpolar foci in the wildtype background (Fig. 4a, 4e,
273 4g). In some cells, a broad GFP-CheW1 zone appeared around the middle of the cell (Fig.
274 4b), which was often detected as a focus (Fig. 4e, 4g), however it clearly does not
275 resemble the foci of normal chemotaxis arrays. Consistent with this, the fluorescence
276 intensity of GFP-CheW1 around the cell outline in Δ*cetZ1* also was not correlated with
277 cell curvature (Fig. 4f).

278 Overexpression of *cetZ1* did not have a substantial impact on the number of GFP-CheW1
279 foci per cell (Fig. 4e), but it did have a moderate influence on the position of foci in the
280 cell (Fig. 4g) and their localization at areas of cell curvature (Fig. 4f, S5d), which is
281 consistent with the moderate reduction in motility (Fig. 1a). The *cetZ1*.E218A GTPase
282 mutant had a similar inhibitory effect on GFP-CheW1 localization as it did on ArlD1-GFP,
283 substantially disrupting cell shape, GFP-CheW1 localization (Fig. 4b, 4g), and its

association with cell curvature (Fig. 4f). Together these observations suggest CetZ1 is a key driver of CheW1 assembly.

Deletion of *cetZ2* had no detected effect on foci number (Fig. 4e) or positioning of GFP-CheW1 (Fig. 4f, 4g). Although overexpression of *cetZ2* caused no clear difference in GFP-CheW1 foci number (Fig. 4e) it resulted in reduced average correlation of GFP-CheW1 fluorescence with curvature (Fig. 4f) and, consistent with this, a moderate redistribution of some of the foci throughout the cells (Fig. 4g). In contrast, expression of *cetZ2*.E212A resulted in a diffuse signal for GFP-CheW1 (Fig. 4b), with the great majority of cells having no detectable GFP-CheW1 foci (Fig. 4e) and there was essentially no clear correlation between fluorescence and cell curvature (Fig. 4f, 4g), similar to the effects of the *cetZ1*.E218A mutant. These results suggest that *cetZ2* is not directly required for the normal assembly of chemotaxis arrays but has the capacity to disrupt their formation when overexpressed, particularly in the GTPase-inactive form that also has dominant effects on cell shape (Fig. 4b).

CheY assembly is highly dependent on CetZ1

Following these observations of the impacts of CetZs on the assembly of archaellum and chemotaxis structures, we next sought to determine whether CetZs also influence the effector protein, CheY, which shuttles between chemosensory arrays and the archaellum base as part of the signal transduction pathway which results in switching of rotation direction of the archaellum. Deletion of *cetZ1* resulted in mainly diffuse localization of CheY-GFP, with some distinct foci at the cell edge remaining (Fig. 5b, 5g). Overexpression of *cetZ1* did not change the localization pattern of CheY-GFP, but it did reduce the frequency of foci (Fig. 5b, 5e-g). As with ArlD1-GFP and GFP-CheW1, expression of *cetZ1*.E218A also produced a sub-population of large and highly irregular cell shapes with multiple CheY-GFP foci (Fig. 5b), but in the majority of cells, CheY-GFP failed to form foci (Fig. 5e).

Deletion of *cetZ2* had no detected effect on assembly or positioning of CheY-GFP (Fig. 5b). Overexpression of *cetZ2* resulted in less CheY-GFP foci per cell, and like GFP-CheW1, the correlation between CheY-GFP localization and cell curvature was reduced. Expression of *cetZ2*.E212A had similar effects as it did on CheW1 assembly (Fig. 5b, e-g, S5f). The CheY-GFP signal was diffuse or weakly centrally located in most of these cells (Fig. 5b, 5g).

Dual localization of CetZ1 and motility marker proteins

To further investigate the relationships between ArlD1, CheW1, and CheY assembly and CetZ1, we investigated the extent of polar co-localization between the motility markers and CetZ1. Vectors for tandem expression of ArlD1-GFP, GFP-CheW1, or CheY-GFP with CetZ1-mCherry (mCh) were generated (pHJB69-71, respectively). The CetZ1-G-mCh fusion (including the flexible Glycine-rich linker) was used here as it complements the motility and shape defects resultant from deletion of *cetZ1* like the CetZ1-G-mTq2 fusion used above [30].

When CetZ1-mCh was produced with either ArlD1-GFP, GFP-CheW1, or CheY-GFP, all four fusions displayed localization patterns in swimming cells equivalent to those observed when they were expressed individually (Fig. 2c, 3a, 4a, 5a, respectively). To

determine the degree to which ArlD1-GFP foci co-occur with CetZ1-mCh foci, each ArlD1-GFP focus was identified and then categorized into one of three patterns with respect to CetZ1-mCh foci (Fig. 6d). This revealed that the majority (73%) of ArlD1-GFP localizations overlapped with a polar focus of CetZ1-mCh (Fig. 6d(ii)), 26% of ArlD1-GFP foci had no detected CetZ1-mCh focus at the same pole (Fig. 6d(i)), and less than 1% were separated from a CetZ1-mCh focus at the same pole (Fig. 6d(iii)). We also counted cell poles with either one or both foci types present (irrespective of their degree of overlap) and found that 13.8% of poles had both ArlD1-GFP and CetZ1-mCh, which was significantly higher than the 8.1% that would be expected based on a random allocation of the individual foci to each pole (Fig. 6g).

Foci co-localization analysis of CetZ1-mCh with GFP-CheW1 (Fig. 6b, e, h) demonstrated that polar CetZ1-mCh foci were less closely associated with GFP-CheW1 foci positioning compared to ArlD-GFP; 40.5% of GFP-CheW1 foci did not overlap with CetZ1-mCh foci, even when located at the same cell pole (Fig. 6e(iii)), and only 40% of GFP-CheW1 foci overlapped with CetZ1-mCh foci (Fig 6e(ii)), and the remaining ~20% of GFP-CheW1 foci showed no CetZ1-mCh focus at the same pole (Fig 6e(i)). This poorer co-localization than with ArlD1-GFP (fig. 6d, 6e) is consistent with the differing localization patterns of the chemotaxis arrays (often subpolar) and archaella (polar) (Fig. 4, 5). Finally, analysis of CheY-GFP foci showed that 82% had an overlapping CetZ1-mCh focus and only 10% had no CetZ1-mCh focus at the same pole (Fig. 6c, f). Both CheW-GFP and CheY-GFP did not show a significant propensity to co-occur with CetZ1-mCh at poles compared to a random allocation (Fig. 6h, i).

Discussion

CetZ tubulin-like proteins have previously been implicated in the control of cell shape and motility in haloarchaea [12]. In *H. volcanii*, development of rod-shaped cell types requires CetZ1 [12,13] and this morphotype is highly correlated with motility [12,15,31]. The rod-shape is expected to provide a faster, more streamlined hydrodynamic shape and improve the directionality of movement during swimming [32]. Additionally, rod-shaped cells have a polarity which is a likely cue for the correct assembly and polar placement of motility machinery. For example, the MinD4 positioning protein oscillates along the long axis of *H. volcanii* cells and dynamically localises at the cell poles, which influences the correct positioning of ArlD1 and CheW1 at or near the poles [27]. In plate-shaped cells, which do not have such polarity, MinD4 patterns tend to breakdown or move in circles instead of oscillate, and while ArlD1 remains assembled and localised, the archaellum filament and chemosensory arrays are not [17,27], supporting the role of cell polarity in the assembly mechanism of these polar motility complexes.

Here, we initially found that although some manipulations of CetZs (Δ*cetZ1* and expression of the dominant mutants *cetZ1*.E218A or *cetZ2*.E212A [12]) exhibited both rod-shape and motility defects [12], overexpression of wildtype *cetZ1* or *cetZ2* resulted in motility changes without affecting the rod cell shape of swimming cells. This suggested that in addition to their role in controlling cell shape, CetZs might contribute to motility through additional mechanisms.

CetZ1 clearly localises to the poles of actively motile rods withdrawn from the soft agar motility medium (e.g. Fig. 2) [12]. This localization pattern differs substantially compared to the longitudinal filaments and highly dynamic foci seen during rod formation and in rods from liquid culture [12,13], and suggests that CetZ1 has an additional role at the poles of motile rods. The CetZ1-mTq2 fusion protein supported the development of rod shape in swimming cells (i.e. it complemented the Δ*cetZ1* background), though motility was still somewhat reduced compared to the untagged CetZ1, suggesting factors beyond the rod shape of swimming cells influence the overall motility phenotype resulting from variants of CetZ1. Based on these observations, we then sought to test the hypothesis that CetZs may contribute to motility by directly recruiting or indirectly promoting the polar assembly of archaella and chemosensory array protein complexes.

Deletion of *cetZ1* or overexpression of *cetZ1* or *cetZ1*.E218A all reduced assembly and polar positioning of the archaellum and chemotaxis marker proteins, ArlD1, CheW1, and CheY. The effects were of varying degrees that were approximately consistent with the magnitude of their motility defects. Importantly, deletion of *cetZ1* caused major defects in the frequency of assembly of the motility marker proteins. Their remaining localization patterns differed substantially, suggesting that the effects of CetZ1 on their localization manifest differently and are not related in a simple way to cell shape. Furthermore, the results of *cetZ1* overexpression suggested that excess CetZ1 interferes with the proper assembly of the motility proteins without changing the rod shape of motile cells. Taken together, these findings strongly suggest that CetZ1 can contribute to motility through shape-independent mechanisms that promote the assembly of the motility machinery, in addition to its essential role in rod formation.

Deletion of *cetZ2* caused no detected defects in motility or assembly of the motility machinery. Although overexpression of *cetZ2* resulted in a mild increase in motility and the number of surface filaments as detected by cellular cryoEM (interpreted as archaella), it appeared to result in somewhat fewer assemblies (foci) of the motility marker proteins at the cell poles. A potential explanation is that *cetZ2* overexpression synthetically promotes clustering of the motility proteins at the cell pole, which are not resolved by fluorescence microscopy. Whether CetZ2 has a natural role in *H. volcanii* motility in standard or other conditions is currently unknown.

How might CetZ1 contribute to the structure of the cell poles and assembly of the motility machinery there? Our dual-localization studies indicated that polar foci of CetZ1 and the motility marker proteins often overlapped but were clearly not always overlapping. In particular, the archaellum marker, ArlD1-GFP, and CetZ1-mCh appeared to have a specific propensity to co-localize at cell poles. However, the imperfect co-localization and partial independence of localization suggests that none of the motility machinery markers form an obligate or stoichiometric co-assembly with CetZ1. Since CetZ1 has a strong impact on assembly of all the motility markers—particularly CheW1 despite showing the lowest polar co-localization with CetZ1 (Fig. 4, 6)—the results suggest that CetZ1 has a distinct function in establishing the structure of the cell pole, which in turn plays a significant role in the proper assembly of the motility machineries.

Polar cap structures have been identified in several archaeal species, including *Thermococcus kodakarensis* [25], *Pyrococcus furiosus* [26], and a closer relative of *H. volcanii*, *Halobacterium salinarum* [33]. Although hypothesized to exist [18], a similar polar cap has not been identified in *H. volcanii*, and the components of the cap structures in other archaea are also not known. Together with the observation that CetZ1 strongly localises at the cell poles of motile cells, our data suggest a new role of CetZ1 as a functional component for the polar cap in *H. volcanii*. CetZ1 appears to polymerize and form protofilaments that can assemble laterally into sheets and are predicted to interact with the inner membrane [12,13]. We predict that such sheet-like structures assemble and help form the structure of the cell poles to promote assembly of motility structures.

Both CetZ1 and CetZ2 have even been identified as potential interacting partners with several chemotaxis proteins (including CheW1 and CheY) by affinity purification and mass spectrometry in *H. salinarum* [34], which is known to have a polar cap [33]. High resolution structural and compositional analysis of cap structures in *H. volcanii* would be valuable towards determining the structural role of CetZ1 at cell poles. With CetZ1 and MinD4 [27] both implicated in the positioning of archaella and chemosensory arrays at cell poles, future research could also investigate how these two proteins coordinate their activities, and where they lie within the hierarchy of proteins contributing to motility.

Our findings represent the first evidence that a CetZ family protein participates in multiple distinct roles, and in promoting the assembly of other proteins at the cell surface. Taken together with the diversity and multiplicity of tubulin superfamily proteins in archaea [1,15], it is likely that similar characteristics in early archaea led to the vast functional complexity, diversity, and specialisation of tubulins in eukaryotes. Our findings are also reminiscent of the fundamental roles of tubulin at the base of the eukaryotic flagellum, which originated before the last eukaryotic common ancestor [35-38]. Since flagellar basal body microtubules are derived from mitotic centrioles during eukaryotic

cell differentiation, it is interesting to consider parallels to *H. volcanii*, where dynamic repositioning of CetZ1 longitudinal filaments during rod formation [12,13] is followed by the formation of polar structures that promote stable assembly of the motility machinery in mature rod cells.

Materials and Methods

Growth and genetic modification of H. volcanii

H. volcanii was routinely grown in Hv-Cab or Hv-YPCab medium [14] supplemented with 50 µg/mL uracil if necessary to fulfil auxotrophic requirements of strains, or with L-Tryptophan to induce expression of genes of interest from pTA962-based [39] expression plasmids. Cultures were grown at 42 °C with shaking (200 rpm). *H. volcanii* was transformed with demethylated plasmids extracted from *E. coli* strain C2925 using the previously described method [40].

H. volcanii H26 (ID621) was used as the wildtype background and as the parent strain of the Δ*cetZ1* (ID622) and Δ*cetZ2* (ID357) strains, which were generated as in-frame deletions of *cetZ1* (HVO_2204) or *cetZ2* (HVO_0745) using the previously described plasmids pTA131_2204_IF [16] and pTA131_CetZ2 [12], respectively and 'pop-in pop-out' method [41]. For all experiments, *H. volcanii* strains contained the pTA962 shuttle vector (control strains) or vectors for expression of relevant genes. Strains are listed in Table S1.

Plasmid construction

All reagents for plasmid construction were obtained from New England Biolabs and used according to the manufacturer's instructions, and oligonucleotides were obtained from Integrated DNA Technologies. Plasmids and oligonucleotides used for cloning detailed in Tables S2 and S3, respectively. To generate a plasmid for the expression of CetZ2-EG-mTurquoise2, the *cetZ2* ORF was amplified from pTA962-CetZ2 using a reverse primer to remove the stop codon and incorporate a BamHI restriction site to the 3' end. The amplified ORF was then ligated between NdeI and BamHI in pHVID21 [16].

For plasmids for dual expression of untagged CetZs and GFP tagged motility proteins, ORFs for ArlD1-GFP, GFP-CheW1, and CheY-GFP were amplified from pSVA3919, pSVA5031, and pSVA5611, respectively, incorporating a BglII restriction site at the 5' end, and a NotI site at the 3' end. After purification and restriction digestion, these ORFs were ligated between BamHI and NotI sites of pTA962-CetZ1, pTA962-CetZ2, pTA962-CetZ1.E218A, and pTA962-CetZ2.E212A, utilising the compatible ends generated by BglII and BamHI. The resulting vectors contained the p.*tna* promotor, immediately followed by the CetZ ORF and then the ArlD1, CheW1, or CheY-GFP fusion ORF which was maintained in-frame. The sequences of all constructed plasmids were confirmed by Sanger sequencing (Australian Genome Research Facility).

Plasmids for tandem expression of CetZ1-mCherry (mCh) and ArlD1-GFP, GFP-CheW1, or CheY-GFP were generated as described previously in [30]. Briefly, ORFs for ArlD1-GFP, GFP-CheW1, and CheY-GFP were amplified from pSVA3919, pSVA5031, and pSVA5611, respectively, introducing an XbaI restriction site at the 5' end. These were ligated between NheI and NotI of pHVID132, the vector containing the CetZ1-G-mCh ORF.

Soft-agar motility assays

To prepare cultures for soft-agar motility assays, single colonies were inoculated into Hv-Cab medium with 1 mM L-Tryptophan and grown to an approximate OD_{600} of 0.6 overnight.

482 Following this, cultures were passaged into fresh Hv-Cab medium with 1 mM L-
483 Tryptophan every 24 hours for three days. All cultures were normalised to the same
484 starting OD_{600} before spotting 2 µL of culture onto the soft agar.

485 Hv-Cab soft-agar containing 1 mM L-Tryptophan was prepared the day before inoculation
486 of cultures onto the agar. For experiments quantifying halo size, 0.25 % (w/v) agar was
487 used, and motility plates were incubated for 3 days at 42 °C. This concentration of agar
488 resulted in better uniformity of halo shape and reproducibility of halo size, which was
489 quantified by taking the mean of two perpendicular measurements of the halo diameter.
490 Motility assays prepared for subsequent microscopy of halo edge cells used 0.3% agar
491 instead, and were incubated for 4-5 days at 42 °C. This method sometimes resulted in
492 irregularly shaped motility halos but produced a more defined leading edge for easier
493 extraction of cells from the agar for analysis by microscopy.

494 ***Light microscopy***

495 Cells were extracted from the edge of motility halos by stabbing the agar with a
496 micropipette (5-10 µL) near the bottom of the agar plate. After pipetting up and down
497 several times to liquify the soft-agar and release the cells, the sample was transferred to
498 a glass slide with a pad containing 1.5 % agarose and 18 % Buffered Salt Water (BSW)[41]
499 before covering with a #1.5 glass coverslip. All phase-contrast and fluorescence
500 microscopy were conducted on the V3 DeltaVision Elite (GE Healthcare) with filter sets
501 for GFP/FITC (excitation=464-492 nm, emission=500-523 nm) and mTurquoise2/CFP
502 (excitation=400-453 nm, emission=463-487 nm), an 100X Olympus UPLSAPO/NA 1.4
503 objective, and pco.edge 5.5 sCMOS camera. Exposure settings were always maintained
504 between all strains expressing the same fusion protein.

505 ***Light microscopy image analysis***

506 To analyse cell shape characteristics and analysis of fluorescence and localization of
507 fluorescent fusion proteins within cells, MicrobeJ v5.13I [42] was used, a plugin for FIJI
508 v2.14.0/1.54f [43]. Unless otherwise mentioned, all settings in MicrobeJ were left as default.
509 Phase-contrast images were used to detect cell outlines using the default thresholding
510 algorithm and a cell area restriction of 1.0-max μm^2. Fluorescent localization was
511 analysed using the *point* detection method. Due to large variance in focus intensity and
512 background fluorescence between genetic backgrounds and plasmids, the tolerance
513 parameter had to be adjusted for each strain as needed for accurate foci detection, but
514 foci detection parameters were maintained between biological replicates. Heatmaps of
515 normalized focus localization were generated using the *XYCellDensity* function, and all
516 other image analysis outputs were extracted from the MicrobeJ results tables.

517 A FIJI macro and Python scripts were written and used to conduct local cell curvature
518 analysis and correlation with fluorescence intensity, based on a previous approach [12]. In
519 short, local curvature was analysed using phase-contrast images and the Contour
520 Curvature v1.1.x (www.gluender.de) plugin in FIJI with the number of contour samples set
521 to 100, and number of coefficient pairs set to 10. The local curvature at each contour
522 sample was recorded, and these values were used to calculate the relative standard
523 deviation (RSD) of curvature for each cell. The mean fluorescence intensity along the cell
524 outline generated by Contour Curvature was measured using a 3-pixel line width and was

correlated with local curvature by calculating the Pearson correlation coefficient between fluorescence intensity and local curvature for each individual cell. A summary of the image acquisition and analysis pipeline for light microscopy is provided in Fig. S4.

To determine the degree to which polar localised motility markers co-occurred or overlapped with CetZ1, 100 foci of each motility marker were manually identified (blind to CetZ1-mCh), and categorized into one of three patterns with respect to CetZ1-mCh foci: (i) no focus of CetZ1-mCh was located at the same cell pole, (ii) the motility marker and CetZ1-mCh foci were fully or partially overlapping, or (iii) the motility marker and CetZ1-mCh foci were located at the same pole but are not overlapping. This was carried out separately for each biological (culture) replicate and the mean (and SEM) were obtained.

Using the same fluorescence datasets, MicrobeJ was used to score the occurrence of CetZ1-mCh, ArlD1-GFP, GFP-CheW1, and CheY-GFP in the polar or sub-polar regions. Cell outlines were detected using the phase-contrast channel as described above, and fluorescent foci were detected using the *point* detection method. For the motility markers (GFP channel), tolerance was set to 200, and for CetZ1-mCh tolerance was set to 100. The number of foci per pole were extracted for each channel (For marker-GFP: *Maxima1.count.pole.1* and *Maxima1.count.pole.2*; and for CetZ1-mCh: *Maxima2.count.pole.1* and *Maxima2.count.pole.2*). These were used to determine the number of poles with either one, or both GFP and mCh foci present. We calculated the expected percentage of cell poles with both marker-GFP and CetZ1-mCh foci assuming their co-occurrence is uncorrelated by multiplying the percentage of total poles with at least one GFP focus by the percentage of total poles with at least one mCh focus. The mean, SD and statistical significance were calculated based on the culture replicates.

Cryo-Electron Microscopy and analysis

To maximize the number of cells per sample for cryo-electron microscopy, cultures were grown from a theoretical starting OD_{600} of 0.0005 in Hv-YPCab [14] medium and harvested at OD_{600}~0.25 (after ~24 hours). A 4.5 µL droplet of the culture was applied to glow discharged copper grids (Quantifoil R2/2, Quantifoil Micro Tools) and blotted for 2.5 s in a 95% humidity chamber at 20 °C. The grids were then plunged into liquid ethane using a Lecia EM GP device. The grids were imaged using a Talos Arctica cryo-TEM (Thermo Fisher Scientific), operating at 200 kV with the specimen held at liquid nitrogen temperature. Images were captured at 17,500X magnification using a Falcon 3EC direct electron detector in linear mode. The number of surface filaments per cell (Fig. 1d, e) was manually counted using Cryo-TEM images. This was conducted independently and blindly by three individuals.

Acknowledgements

The authors would like to acknowledge S. Albers for providing strains and plasmids, as well as L. Cole and A. Bottomley from the UTS Microbial Imaging Facility. We acknowledge the use of the Cryo-Electron Microscopy Facility through the Victor Chang Cardiac Research Institute Innovation Centre, funded by the NSW government and the Electron Microscope Unit within the Mark Wainwright Analytical Centre (MWAC) at UNSW Sydney. The work was supported by the Australian Research Council (DP160101076 and FT160100010 to IGD).

Author contributions

Conceptualisation – HJB & IGD; Data curation – HJB, MII & JR; Formal analysis – HJB, MII & JR; Investigation – HJB, MII, JR; Methodology – all authors; Supervision – IGD, SI & MABB; Original draft – HJB; Revision – HJB & IGD; Reviewing the manuscript – all authors. Funding Acquisition – IGD.

References

1. Aylett, C.H., and Duggin, I.G. (2017). The tubulin superfamily in archaea. In Prokaryotic Cytoskeletons, (Springer), pp. 393-417.
2. Nogales, E., Downing, K.H., Amos, L.A., and Löwe, J. (1998). Tubulin and FtsZ form a distinct family of GTPases. Nature Structural and Molecular Biology *5*, 451.
3. Vaughan, S., Wickstead, B., Gull, K., and Addinall, S.G. (2004). Molecular evolution of FtsZ protein sequences encoded within the genomes of archaea, bacteria, and eukaryota. Journal of molecular evolution *58*, 19-29.
4. Erickson, H.P. (2007). Evolution of the cytoskeleton. Bioessays *29*, 668-677.
5. Erickson, H.P. (1995). FtsZ, a prokaryotic homolog of tubulin? Cell *80*, 367-370.
6. Barton, N.R., and Goldstein, L. (1996). Going mobile: microtubule motors and chromosome segregation. Proceedings of the National Academy of Sciences *93*, 1735-1742.
7. Appert-Rolland, C., Ebbinghaus, M., and Santen, L. (2015). Intracellular transport driven by cytoskeletal motors: General mechanisms and defects. Physics Reports *593*, 1-59.
8. Hirokawa, N., Noda, Y., Tanaka, Y., and Niwa, S. (2009). Kinesin superfamily motor proteins and intracellular transport. Nature reviews Molecular cell biology *10*, 682-696.
9. An, S., Deng, Y., Tomsho, J.W., Kyoung, M., and Benkovic, S.J. (2010). Microtubule-assisted mechanism for functional metabolic macromolecular complex formation. Proceedings of the National Academy of Sciences *107*, 12872-12876.
10. Hawkins, T., Mirigian, M., Yasar, M.S., and Ross, J.L. (2010). Mechanics of microtubules. Journal of biomechanics *43*, 23-30.
11. Lutkenhaus, J., Pichoff, S., and Du, S. (2012). Bacterial cytokinesis: from Z ring to divisome. Cytoskeleton *69*, 778-790.
12. Duggin, I.G., Aylett, C.H., Walsh, J.C., Michie, K.A., Wang, Q., Turnbull, L., Dawson, E.M., Harry, E.J., Whitchurch, C.B., and Amos, L.A. (2015). CetZ tubulin-like proteins control archaeal cell shape. Nature *519*, 362.
13. de Silva, R.T., Shinde, V., Brown, H.J., Liao, Y., and Duggin, I.G. (2024). Dynamic self-association of archaeal tubulin-like protein CetZ1 drives Haloferax volcanii morphogenesis. bioRxiv, 2024.2004. 2008.588506.
14. de Silva, R.T., Abdul-Halim, M.F., Pittrich, D.A., Brown, H.J., Pohlschroder, M., and Duggin, I.G. (2021). Improved growth and morphological plasticity of Haloferax volcanii. Microbiology. 10.1099/mic.0.001012.
15. Brown, H.J., and Duggin, I.G. (2023). Diversity and Potential Multifunctionality of Archaeal CetZ Tubulin-like Cytoskeletal Proteins. Biomolecules *13*, 134.
16. Ithurbide, S., de Silva, R.T., Brown, H.J., Shinde, V., and Duggin, I.G. (2024). A vector system for single and tandem expression of cloned genes and multi-colour fluorescent tagging in Haloferax volcanii. bioRxiv, 2024.2003. 2013.584740.
17. Li, Z., Kinosita, Y., Rodriguez-Franco, M., Nußbaum, P., Braun, F., Delpech, F., Quax, T.E., and Albers, S.-V. (2019). Positioning of the motility machinery in halophilic archaea. MBio *10*, e00377-00319.
18. Li, Z., Rodriguez‐Franco, M., Albers, S.V., and Quax, T.E. (2020). The switch complex ArlCDE connects the chemotaxis system and the archaellum. Molecular microbiology *114*, 468-479.
19. Quax, T.E., Altegoer, F., Rossi, F., Li, Z., Rodriguez-Franco, M., Kraus, F., Bange, G., and Albers, S.-V. (2018). Structure and function of the archaeal response regulator CheY. Proceedings of the National Academy of Sciences *115*, E1259-E1268.
20. Albers, S.-V., and Jarrell, K.F. (2015). The archaellum: how Archaea swim. Frontiers in Microbiology *6*, 23.
21. Jarrell, K.F., and Albers, S.-V. (2012). The archaellum: an old motility structure with a new name. Trends in microbiology *20*, 307-312.
22. Jarrell, K.F., Albers, S.-V., and Machado, J. (2021). A comprehensive history of motility and Archaellation in Archaea. FEMS Microbes *2*.
23. Albers, S.-V., and Jarrell, K.F. (2018). The archaellum: an update on the unique archaeal motility structure. Trends in microbiology *26*, 351-362.
24. Beeby, M., Ferreira, J.L., Tripp, P., Albers, S.-V., and Mitchell, D.R. (2020). Propulsive nanomachines: the convergent evolution of archaella, flagella and cilia. FEMS microbiology reviews *44*, 253-304.
25. Briegel, A., Oikonomou, C.M., Chang, Y.W., Kjær, A., Huang, A.N., Kim, K.W., Ghosal, D., Nguyen, H.H., Kenny, D., and Ogorzalek Loo, R.R. (2017). Morphology of the archaellar

motor and associated cytoplasmic cone in Thermococcus kodakaraensis. EMBO reports *18*, 1660-1670.

26. Daum, B., Vonck, J., Bellack, A., Chaudhury, P., Reichelt, R., Albers, S.-V., Rachel, R., and Kühlbrandt, W. (2017). Structure and in situ organisation of the Pyrococcus furiosus archaellum machinery. Elife *6*, e27470.
27. Nußbaum, P., Ithurbide, S., Walsh, J.C., Patro, M., Delpech, F., Rodriguez-Franco, M., Curmi, P.M., Duggin, I.G., Quax, T.E., and Albers, S.-V. (2020). An oscillating MinD protein determines the cellular positioning of the motility machinery in archaea. Current Biology *30*, 4956-4972. e4954.
28. Kupper, J., Marwan, W., Typke, D., Grünberg, H., Uwer, U., Gluch, M., and Oesterhelt, D. (1994). The flagellar bundle of Halobacterium salinarium is inserted into a distinct polar cap structure. Journal of bacteriology *176*, 5184-5187.
29. Prelich, G. (2012). Gene overexpression: uses, mechanisms, and interpretation. Genetics *190*, 841-854.
30. Ithurbide, S., de Silva, R.T., Brown, H.J., Shinde, V., and Duggin, I.G. (2024). A vector system for single and tandem expression of cloned genes and multi-colour fluorescent tagging in Haloferax volcanii. Microbiology *170*. https://doi.org/10.1099/mic.0.001461.
31. Schwarzer, S., Rodriguez-Franco, M., Oksanen, H.M., and Quax, T.E. (2021). Growth phase dependent cell shape of Haloarcula. Microorganisms *9*, 231.
32. Young, K.D. (2006). The selective value of bacterial shape. Microbiology and molecular biology reviews *70*, 660-703.
33. Mormile, M.R., Biesen, M.A., Gutierrez, M.C., Ventosa, A., Pavlovich, J.B., Onstott, T.C., and Fredrickson, J.K. (2003). Isolation of Halobacterium salinarum retrieved directly from halite brine inclusions. Environmental Microbiology *5*, 1094-1102.
34. Schlesner, M., Miller, A., Besir, H., Aivaliotis, M., Streif, J., Scheffer, B., Siedler, F., and Oesterhelt, D. (2012). The protein interaction network of a taxis signal transduction system in a halophilic archaeon. BMC microbiology *12*, 1-20.
35. Carvalho-Santos, Z., Azimzadeh, J., Pereira-Leal, J.B., and Bettencourt-Dias, M. (2011). Evolution: Tracing the origins of centrioles, cilia, and flagella. J Cell Biol *194*, 165-175. 10.1083/jcb.201011152.
36. Mitchell, D.R. (2007). The evolution of eukaryotic cilia and flagella as motile and sensory organelles. Adv Exp Med Biol *607*, 130-140. 10.1007/978-0-387-74021-8_11.
37. Moran, J., McKean, P.G., and Ginger, M.L. (2014). Eukaryotic Flagella: Variations in Form, Function, and Composition during Evolution. BioScience *64*, 1103-1114. 10.1093/biosci/biu175.
38. Loreng, T.D., and Smith, E.F. (2017). The Central Apparatus of Cilia and Eukaryotic Flagella. Cold Spring Harb Perspect Biol *9*. 10.1101/cshperspect.a028118.
39. Allers, T., Barak, S., Liddell, S., Wardell, K., and Mevarech, M. (2010). Improved strains and plasmid vectors for conditional overexpression of His-tagged proteins in Haloferax volcanii. Applied and environmental microbiology *76*, 1759-1769.
40. Cline, S.W., Lam, W.L., Charlebois, R.L., Schalkwyk, L.C., and Doolittle, W.F. (1989). Transformation methods for halophilic archaebacteria. Canadian Journal of Microbiology *35*, 148-152.
41. Allers, T., Ngo, H.-P., Mevarech, M., and Lloyd, R.G. (2004). Development of additional selectable markers for the halophilic archaeon Haloferax volcanii based on the leuB and trpA genes. Applied and environmental microbiology *70*, 943-953.
42. Ducret, A., Quardokus, E.M., and Brun, Y.V. (2016). MicrobeJ, a tool for high throughput bacterial cell detection and quantitative analysis. Nature microbiology *1*, 1-7.
43. Schindelin, J., Arganda-Carreras, I., Frise, E., Kaynig, V., Longair, M., Pietzsch, T., Preibisch, S., Rueden, C., Saalfeld, S., and Schmid, B. (2012). Fiji: an open-source platform for biological-image analysis. Nature methods *9*, 676.

Figures

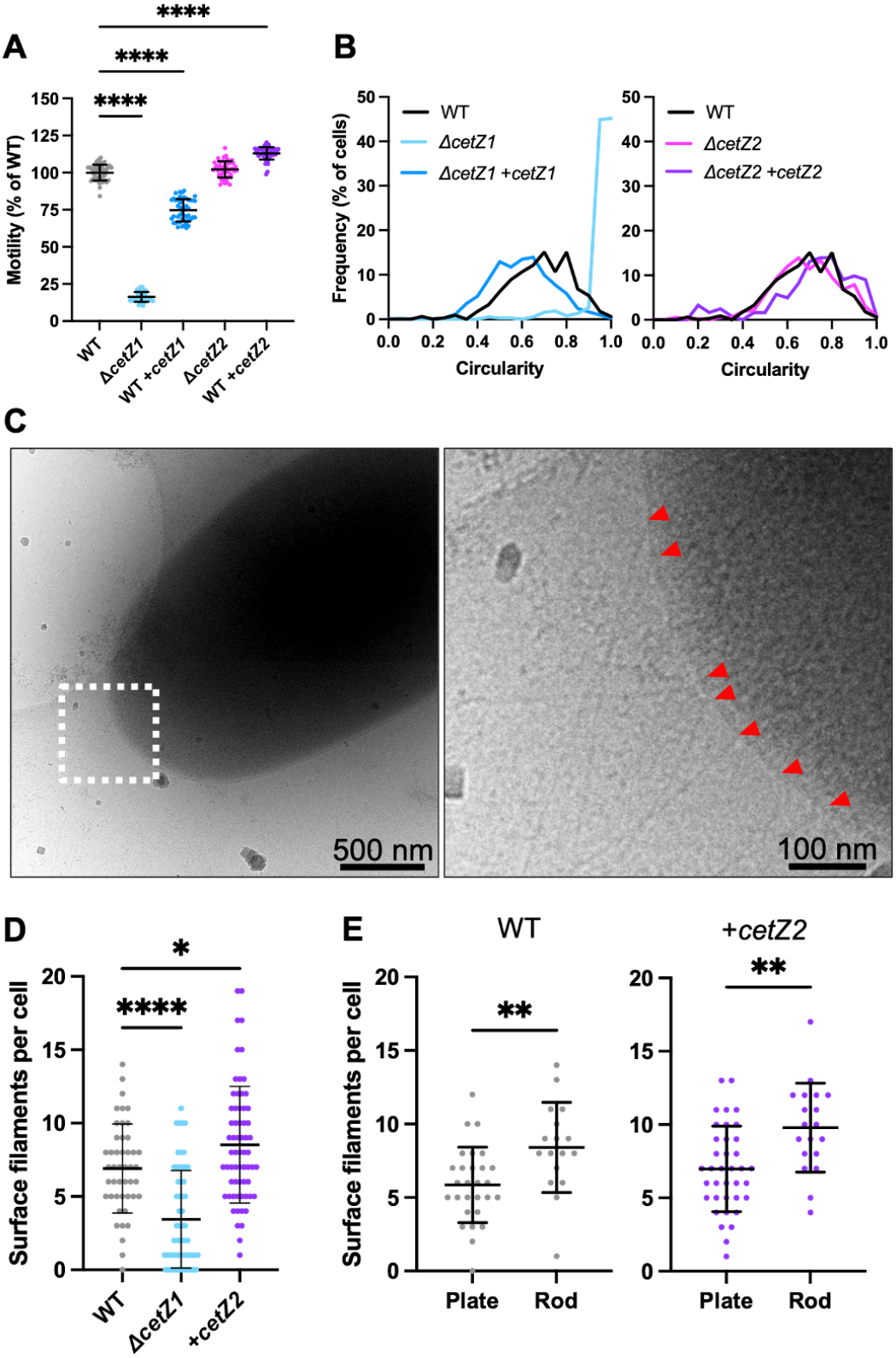

Figure 1. Surface filament assembly in motile cells and CetZ mutants. H26 wildtype, Δ*cetZ1* and Δ*cetZ2* strains with pTA962 vector only, and wildtype with *cetZ1* or *cetZ2* expressed from pTA962 as indicated (+*cetZ1/2*) were inoculated onto Hv-Cab soft-agar with 1 mM L-Tryptophan. **A)** Their motility halo diameters were quantified after four days and normalized to the mean of WT *H. volcanii* H26. Individual points represent biological replicates. **B)** . Circularity of individual cells extracted from the edge of motility halos

was measured and is represented as a frequency distribution for wildtype and knockout *cetZ* strains with pTA962. *cetZ1* and *cetZ2* (+*cetZ1/2*) were expressed in their respective knockout backgrounds. Data for WT +pTA962 is displayed on both graphs for reference. The number of individual cells analysed for each strain is noted in Fig. S1. **C)** Representative CryoEM image of H26 wildtype cells (left) and zoom (right) showing surface filaments (red tick marks). **D)** The number of surface filaments per cell were manually counted using images obtained in **C** for H26 wildtype, Δ*cetZ1*, and +*cetZ2* strains. The number of cells analysed per strain is as follows: WT +pTA962, n=46; Δ*cetZ1* +pTA962, n=58; WT +*cetZ2*, n=66. **E)** For rod forming strains, WT and +*cetZ2*, the number of surface filaments per cell was determined for rod and plate-shaped cells. Data in **D** and **E** was obtained from the same samples. **A, D,** and **E** show mean and standard deviation. **A** and **D** use one-way ANOVA as a statistical test, and **E** uses an un-paired T-test. ****$p<0.00005$, **$p<0.005$, *$p<0.05$.

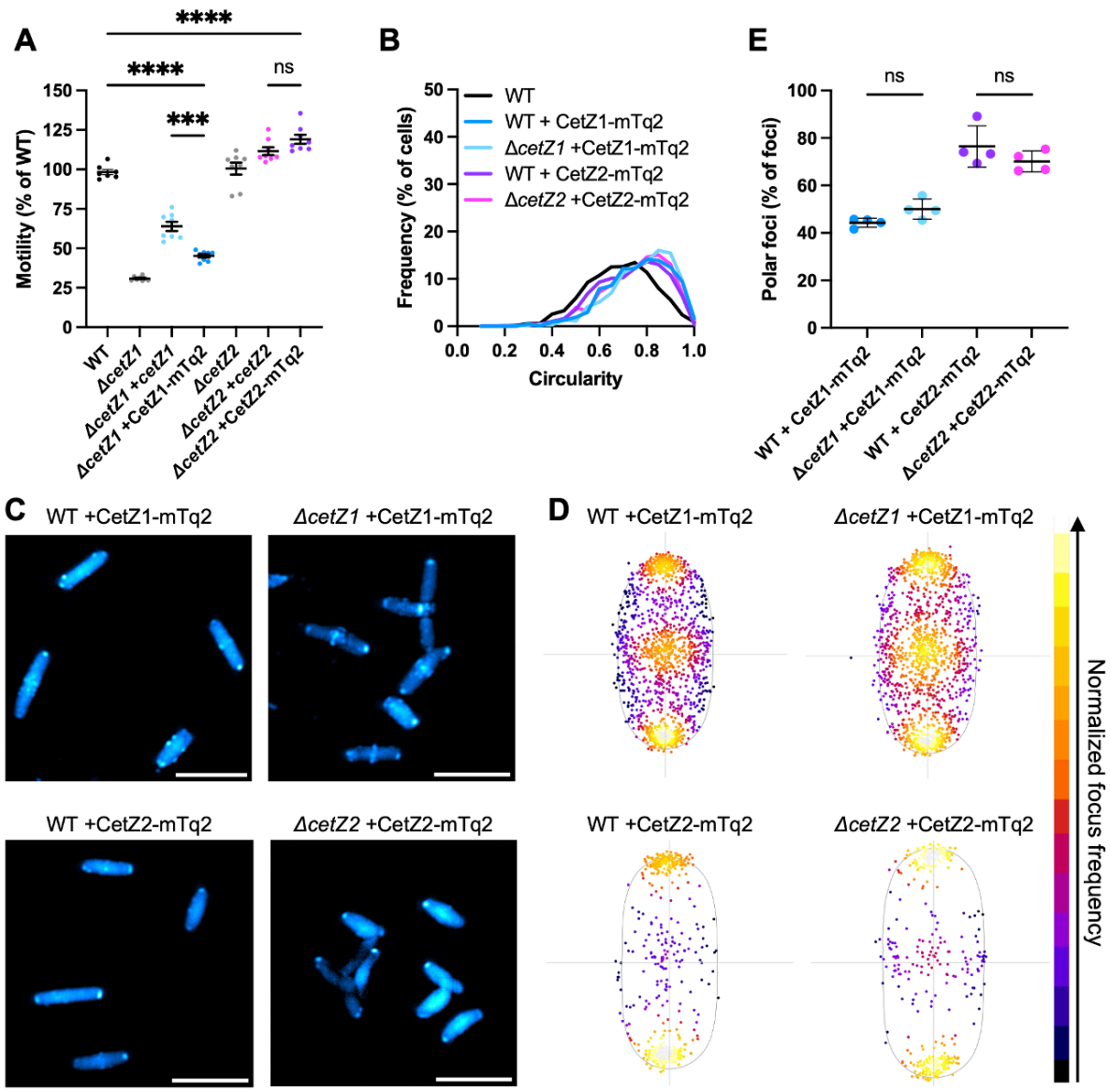

Figure 2. Localization of CetZ1 and CetZ2 in motile cells. CetZ1-mTq2 and CetZ2-mTq2 fusion proteins were produced in H26 wildtype cells and their respective knockout backgrounds. H26 wildtype, Δ*cetZ1,* and Δ*cetZ2* with pTA962, and Δ*cetZ1* +*cetZ1,* and Δ*cetZ2* + *cetZ2* were used as controls. **A)** Strains were inoculated onto Hv-Cab soft-agar with 1 mM L-Tryptophan and their motility halo diameters were quantified. Individual points represent biological replicates. **(B)** Cells expressing *cetZ1* or *cetZ2*-mTq2 fusions were extracted from the edge of the motility halo and their circularity was measured using phase-contrast microscopy images (not shown). **C)** Fluorescence microscopy was also conducted to observe CetZ1 and CetZ2 localization in these cells. **D)** Heatmap representations of CetZ1 and CetZ2 localization in motile cells. **E)** Proportion of detected CetZ foci located at cell poles. In **A** and **E**, mean and standard deviation are shown. One-way ANOVA was used as a statistical test, and only significant and/or relevant comparisons are shown on graphs. ****p<0.00005, ***p<0.0005, ns=not significant. The number of cells analysed for each strain in **B-E** was as follows: WT +pTA962, n=2046; WT +CetZ1-mTq2, n=1193; Δ*cetZ1* +CetZ1-mTq2, n=1672; WT +CetZ2-mTq2, n=1338; Δ*cetZ2* +CetZ2-mTq2, n=861.

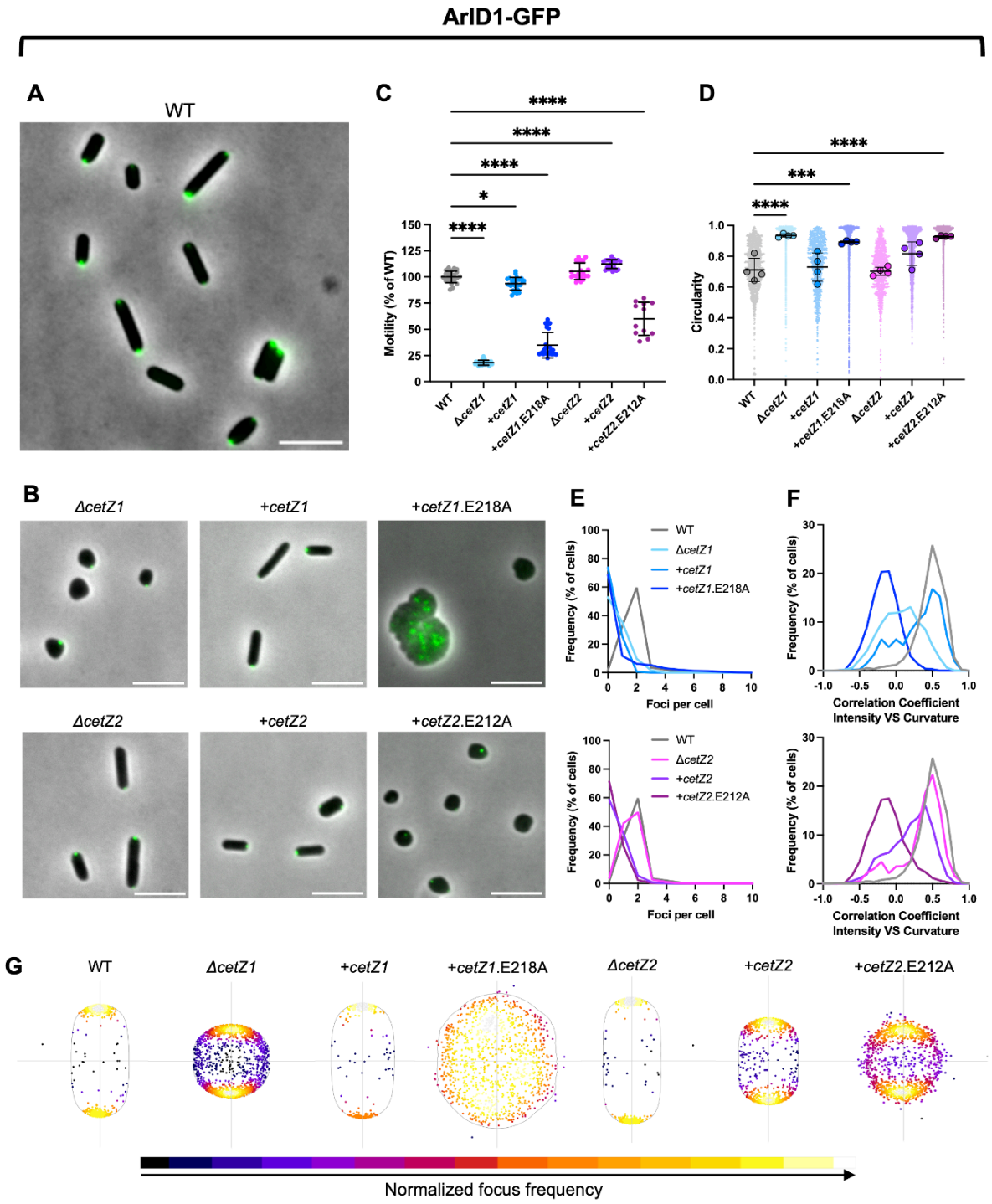

Figure 3. ArlD1-GFP localization in *cetZ1/2* mutant strains. ArlD1-GFP was produced from pSVA3919 in H26 wildtype, Δ*cetZ1*, and Δ*cetZ2*, or was co-expressed with *cetZ1*, *cetZ1*.E218A, *cetZ2*, or *cetZ2*.E212A from pHJB31, pHJB34, pHJB37, or pHJB40, respectively, in H26 wildtype. These strains were inoculated onto Hv-Cab soft-agar with 1 mM L-Tryptophan and extracted from the halo-edge for phase-contrast and fluorescence microscopy **(A, B)**. Four biological replicates were carried out for each strain. Scale bar: 5 µm. **C)** Motility halo diameters for each strain were quantified. Individual points represent biological replicates. Mean and standard deviation is shown. **D)** Phase-contrast images were used to measure circularity. Large individual points represent the mean of all cell circularities in a biological replicate, and small individual points represent individual cells. Mean and standard deviation of replicate means are shown. One-way ANOVA was used as a statistical test (comparing replicate means in **D**). ****p<0.00005, ***p<0.0005, **p<0.005, *p<0.05. Only significant comparisons are shown. **E)** Frequency distributions of the number of foci per cell in each strain, and **F)** the Pearson Correlation Coefficient between local membrane curvature

733 and fluorescence intensity. In **E** and **F**, data for WT +ArlD1-GFP is displayed on all graphs for reference, and
734 the key refers to both panels. **G)** Heatmap representations of ArlD1-GFP foci frequency with respect to the
735 average cell shape normalized by the two major cell axes, in the indicated strain backgrounds. For **D-G** the
736 number of cells pooled from all biological replicates for each strain is as follows: WT +ArlD1-GFP, n=2240;
737 Δ*cetZ1* +ArlD1-GFP, n=1097; WT +*cetZ1* +ArlD1-GFP, n=1448; WT +*cetZ1*.E218A +ArlD1-GFP, n=2007;
738 Δ*cetZ2* +ArlD1-GFP, n=1249; WT +*cetZ2* +ArlD1-GFP, n=1655; WT +*cetZ2*.E212A +ArlD1-GFP, n=1466.

739

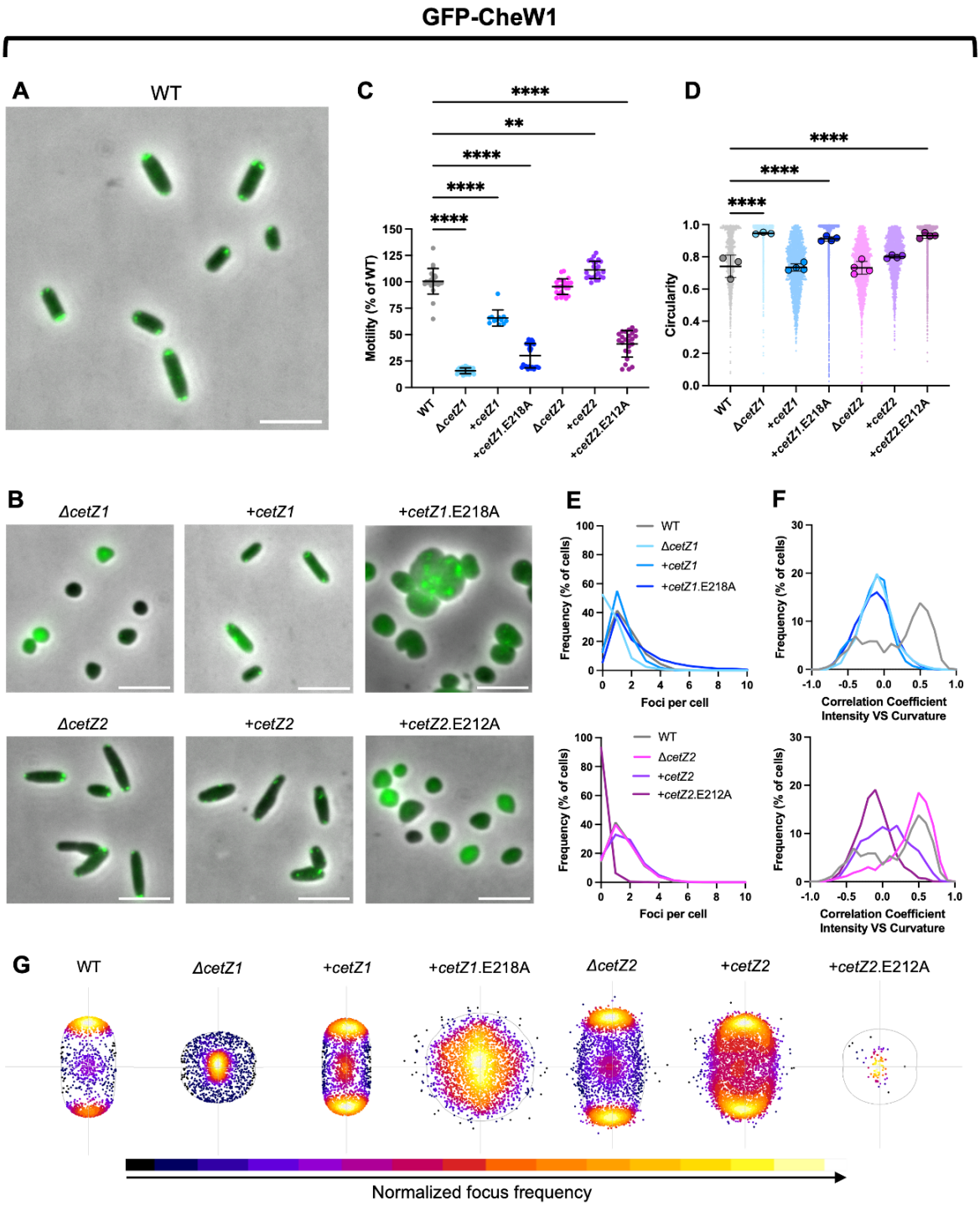

Figure 4. GFP-CheW1 localization in *cetZ1/2* mutant strains. GFP-CheW1 was produced from pSVA5031 in H26 wildtype, Δ*cetZ1*, and Δ*cetZ2*, or was co-expressed with *cetZ1*, *cetZ1*.E218A, *cetZ2*, or *cetZ2*.E212A from pHJB32, pHJB35, pHJB38, or pHJB41, respectively, in H26 wildtype. These strains were inoculated onto Hv-Cab soft-agar with 1 mM L-Tryptophan and extracted from the halo-edge. **A-G** is as described in Figure 3. For **D-G** the number of cells pooled from all biological replicates for each strain is as follows: WT +GFP-CheW1, n=1792; Δ*cetZ1* +GFP-CheW1, n=2458; WT +*cetZ1* +GFP-CheW1, n=2195; WT +*cetZ1*.E218A +GFP-CheW1, n=3834; Δ*cetZ2* +GFP-CheW1, n=3222; WT +*cetZ2* +GFP-CheW1, n=2121; WT +*cetZ2*.E212A +GFP-CheW1, n=4055.

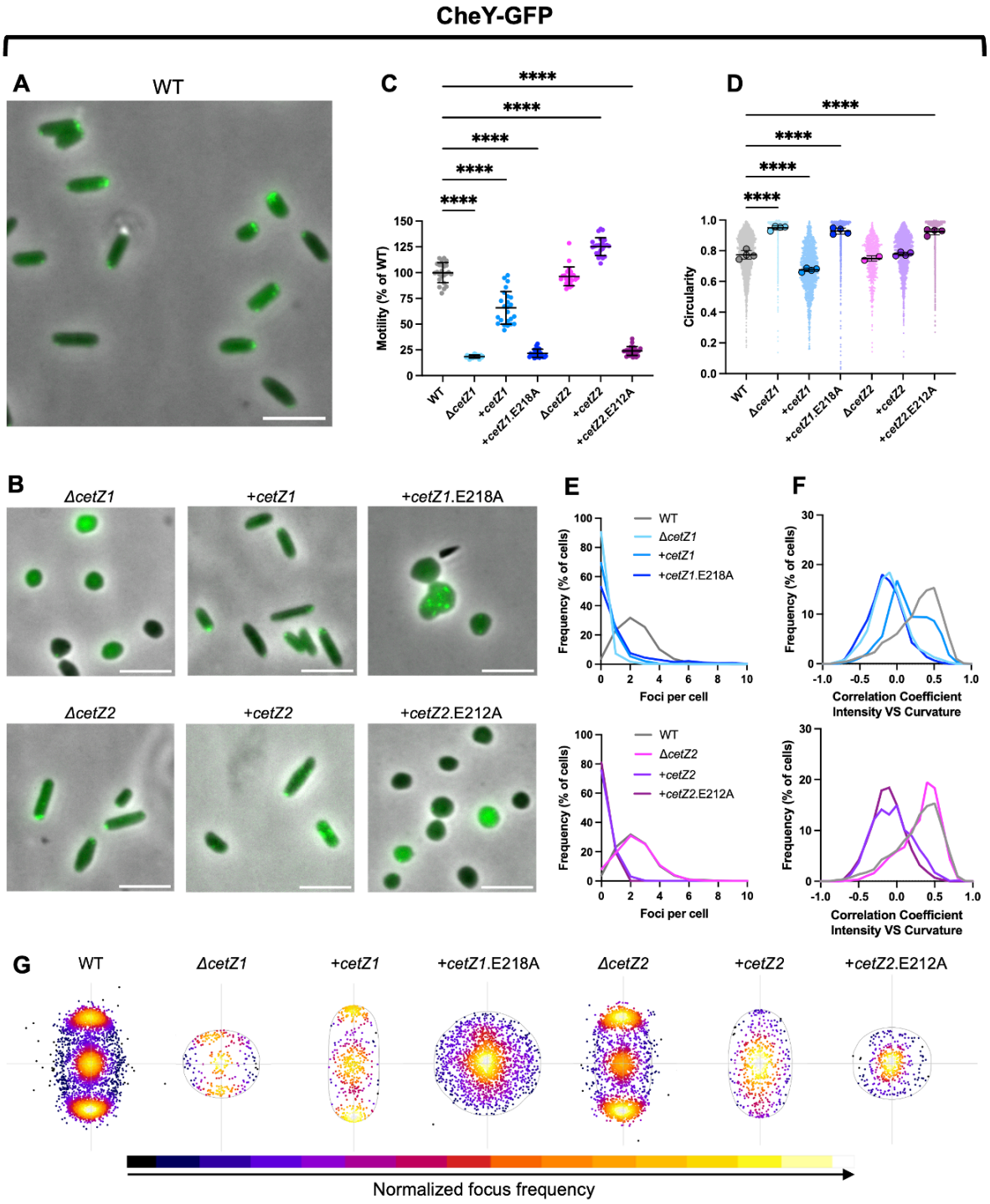

Figure 5. CheY-GFP localization in *cetZ1/2* mutant strains. CheY-GFP was produced from pSVA5611 in H26 wildtype, Δ*cetZ1*, and Δ*cetZ2*, or was co-expressed with *cetZ1*, *cetZ1*.E218A, *cetZ2*, or *cetZ2*.E212A from pHJB33, pHJB36, pHJB39, or pHJB42, respectively, in H26 wildtype. These strains were inoculated onto Hv-Cab soft-agar with 1 mM L-Tryptophan and extracted from the halo-edge. **A-G** is as described in Figure 3. For **D-G** the number of cells pooled from all biological replicates for each strain is as follows: WT +CheY-GFP, n=2892; Δ*cetZ1* +CheY-GFP, n=1825; WT +*cetZ1* +CheY-GFP, n=1490; WT +*cetZ1*.E218A +CheY-GFP, n=1704; Δ*cetZ2* +CheY-GFP, n=1341; WT +*cetZ2* +CheY-GFP, n=1833; WT +*cetZ2*.E212A +CheY-GFP, n=2422.

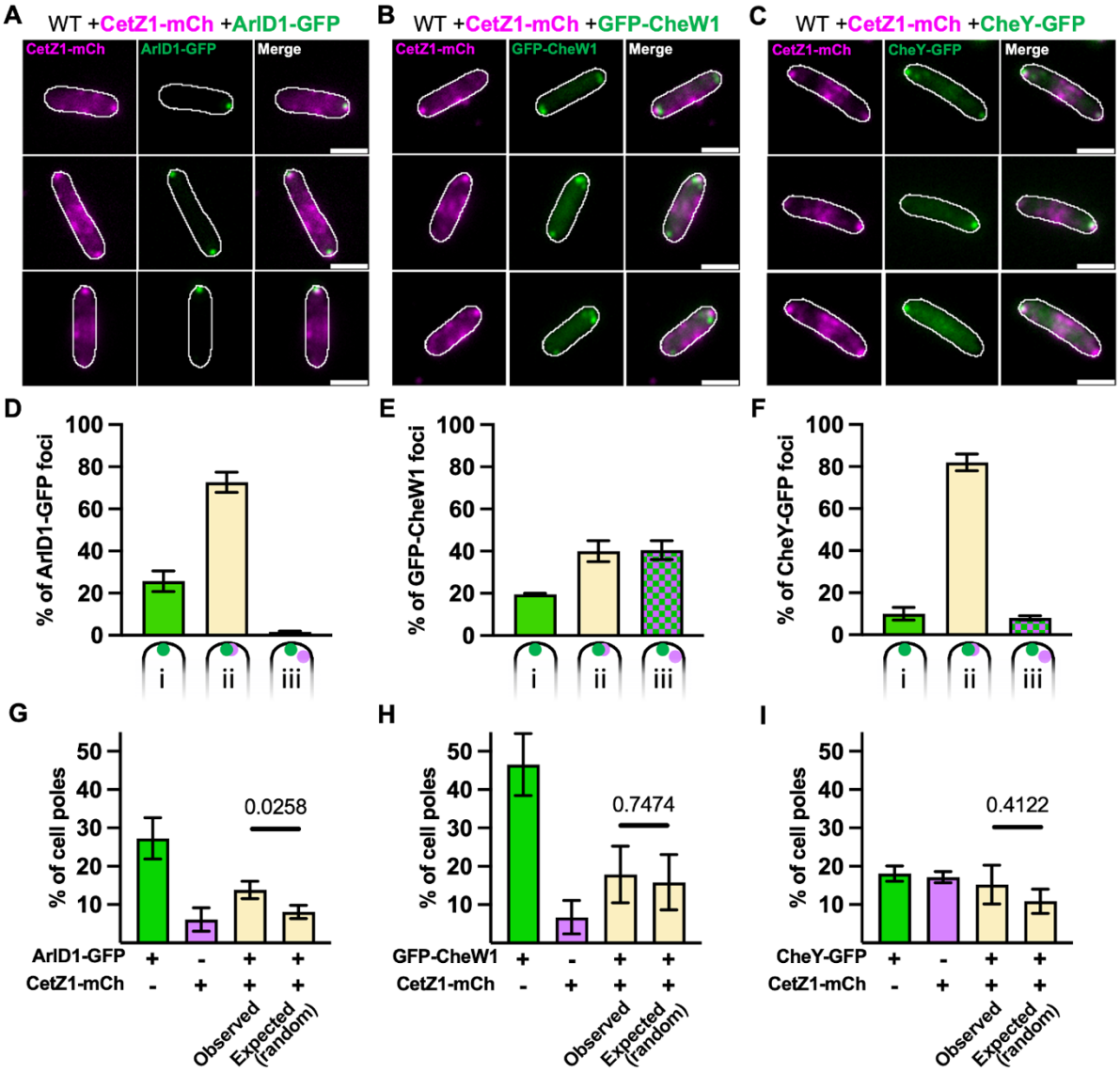

Figure 6. Dual localization of CetZ1-mCherry with ArlD1, CheW1 and CheY GFP fusions. A) ArlD1-GFP, **B)** GFP-CheW1, or **C)** CheY-GFP were produced in tandem with CetZ1-mCh in H26 wildtype cells from plasmids pHJB69, pHJB70, and pHJB71, respectively. Cells were inoculated onto Hv-Cab soft-agar with 1 mM L-Tryptophan and extracted from the halo-edge for fluorescence microscopy. At least two culture replicates were carried out for each strain. To assess the degree of CetZ1-mCh localisation at cell poles with a localised motility marker, 100 foci of motility marker proteins were first identified without viewing CetZ1-mCh localization for each culture replicate. Then the selected foci of **D)** ArlD1-GFP, **E)** GFP-CheW1, and **F)** CheY-GFP were classed in one of three categories: (i) no focus of CetZ1-mCh detected at the same pole, (ii) overlapping (fully or partially) with CetZ1-mCh focus; or (iii) not overlapping with a CetZ1-mCh focus detected at the same cell pole. For **D-F**, mean and standard error is shown (n=3 cultures for **D** and **E**, n=2 cultures for **F**). The presence or absence of CetZ1-mCh, **G)** ArlD1-GFP, **H)** GFP-CheW1, and **I)** CheY-GFP was scored at each cell pole across the entire population. This was conducted separately for each biological (culture) replicate, and presence/absence data is represented as a percentage of cell poles. '+' indicates present, '-' indicates absent. **G-I)** show mean and standard deviation (n=3 cultures for **G** and **H**, n=2 cultures for **I**). A two-tailed T-test was conducted to statistically compare the observed and expected proportions of cell poles with both the motility marker and CetZ1-mCh. The resulting p-values are shown.